frontiers | Frontiers in Earth Science

TYPE Original Research
PUBLISHED 29 July 2025
DOI 10.3389/feart.2025.1655963

Check for updates

OPEN ACCESS

EDITED BY
Chen Zhao,
Shenyang Center of China Geological Survey, China

REVIEWED BY
Xu Xiaofei,
Kunming University of Science and Technology, China
Xisong Zhang,
China University of Mining and Technology, China

*CORRESPONDENCE
Zhanzhan Duan,
duanzhan@pku.edu.cn
Wei Cui,
cui_wei1025@163.com

RECEIVED 29 June 2025
ACCEPTED 14 July 2025
PUBLISHED 29 July 2025

CITATION
Zu D, Duan Z, Cui W, Yang L, Liu J, Tian Z and Zhang J (2025) Geochronology and metamorphic evolution of the biotite-plagioclase gneisses from the Luanxian Group in eastern Hebei, North China Craton.
Front. Earth Sci. 13:1655963.
doi: 10.3389/feart.2025.1655963

COPYRIGHT
© 2025 Zu, Duan, Cui, Yang, Liu, Tian and Zhang. This is an open-access article distributed under the terms of the Creative Commons Attribution License (CC BY). The use, distribution or reproduction in other forums is permitted, provided the original author(s) and the copyright owner(s) are credited and that the original publication in this journal is cited, in accordance with accepted academic practice. No use, distribution or reproduction is permitted which does not comply with these terms.

Geochronology and metamorphic evolution of the biotite-plagioclase gneisses from the Luanxian Group in eastern Hebei, North China Craton

Daji Zu[1], Zhanzhan Duan[1]*, Wei Cui[2]*, Liqun Yang[2], Jia Liu[2], Zhiqiang Tian[2] and Juquan Zhang[1]

[1]Hebei Province Collaborative Innovation Center for Strategic Critical Mineral Research, College of Earth Sciences, Hebei GEO University, Shijiazhuang, China, [2]The 2nd Geological Brigade of Hebei Bureau of Geology and Mineral Resource Exploration, Tangshan, China

Previous metamorphic studies in the eastern Hebei terrane have predominantly focused on rocks within gneiss domes and the Saheqiao linear tectonic belt, while the metamorphosed supracrustal rocks of the Luanxian Group in the Lulong-Shuangshanzi supracrustal belt between gneiss domes remain insufficiently investigated, with limited understanding of their metamorphic characteristics and tectonic setting. This study conducts detailed field investigations, petrological observations, phase equilibria modelling, and zircon U–Pb geochronology on biotite-plagioclase gneisses (samples N16-1 and N16-6) from the Sijiaying iron deposit area. Sample N16-1 contains a mineral assemblage dominated by biotite, K-feldspar, plagioclase, quartz, and epidote, with minor muscovite and sphene, where the minimum X_{An} in plagioclase (0.20) and maximum X_{Ti} in biotite (0.102) constrain peak metamorphic conditions to ~7.4 kbar/586°C in the phase diagram. Chemical composition zoning with increasing X_{Ti} from core to rim in biotite indicates a pre-peak P–T increase process. Sample N16-6 exhibits a mineral assemblage of biotite, plagioclase, K-feldspar, muscovite, and quartz, with epidote and albite occurring as inclusions in biotite, where peak P–T conditions of ~7.0 kbar/630°C are defined by X_{An} (0.174) in plagioclase and X_{Ti} (0.104) in biotite. Post-peak decompression-cooling is defined by decreasing X_{Ti} from core to rim in matrix biotite, collectively defining a clockwise P–T path. Whole-rock geochemical data suggest that the protoliths of the metamorphic supracrustal rocks are pelite and/or greywacke. LA-ICP-MS zircon U–Pb dating yields weighted mean $^{207}Pb/^{206}Pb$ ages of 2,547 ± 14 Ma (MSWD = 0.32) and 2,555 ± 14 Ma (MSWD = 0.30) for samples N16-1 and N16-6, respectively. The age of ~2.55 Ga is considered as the maximum depositional timing of supracrustal protoliths, synchronous with TTG gneiss magmatism and regional amphibolite-facies metamorphism.

Integrating previous studies with the geological observations of "dome-and-keel" architecture, near-synchronous magmatism, sedimentation, and metamorphism, as well as characteristic P–T paths, we propose that the eastern Hebei terrane was dominated by a vertical tectonic regime during the Neoarchean.

KEYWORDS

eastern Hebei, phase equilibria modelling, metamorphic P-T paths, zircon U-Pb dating, North China Craton

1 Introduction

The Archean cratons are predominantly composed of tonalite-trondhjemite-granodiorite (TTG) gneisses with minor supracrustal rocks (Condie, 1981), wherein the supracrustal sequences can be categorized into two types based on their occurrences. The first type forms synformal supracrustal belts (commonly termed greenstone belts) that are distributed between dome-shaped granitoid batholiths, collectively constituting the characteristic "dome and keel" architecture (Campbell and Hill, 1988; Collins et al., 1998; Lin et al., 2013; François et al., 2014; Wang et al., 2025), while the second type occurs as rafts or enclaves within the domal granitoids (Duan et al., 2017; Yang and Wei, 2017a; 2017b; Liu et al., 2020; Zhao et al., 2021; Yu et al., 2022). The former one predominantly records greenschist- to amphibolite-facies metamorphism, whereas the metamorphic grade of the latter one exhibits a negative correlation with enclave dimensions. The larger supracrustal blocks typically preserve lower-grade metamorphic assemblages while smaller blocks attain higher metamorphic conditions, even reaching up to ultrahigh-temperature (UHT) metamorphism (Jayananda et al., 2012; Lin and Beakhouse, 2013; Duan et al., 2017; Sizova et al., 2018; Liu et al., 2024). Supracrustal sequences metamorphosed under greenschist- to amphibolite-facies conditions generally exhibit clockwise P–T paths (Stevens, 2002; Diener et al., 2005; Dziggel et al., 2006; Cutts et al., 2014; Liu et al., 2020), whereas those subjected to granulite- to ultrahigh-temperature granulite-facies metamorphism are predominantly characterized by counterclockwise P–T paths (Kwan et al., 2016; Duan et al., 2017; Yang and Wei, 2017a; Liu et al., 2022; Cui et al., 2024).

The Early Precambrian metamorphic basement of the North China Craton is considered to have been assembled through continent-continent or arc-continent collisions of multiple microblocks, though controversies persist regarding the timing of cratonization, subdivision of microblocks, and collision-amalgamation mechanisms (Wu et al., 1998; Zhao et al., 2005; 2012; Zhai and Santosh, 2011; Zhao and Zhai, 2013; Kusky et al., 2016; 2022; Wei et al., 2023). A prevailing model proposes that the metamorphic basement comprises four continental blocks and three Paleoproterozoic orogenic belts (Figure 1a), wherein the Yinshan and Ordos Blocks collided at ~1.95 Ga to form the Western Block and the Khondalite Belt, while the Longgang and Langrim Blocks amalgamated at ~1.95 Ga to establish the Eastern Block and the Jiao-Liao-Ji Belt, culminating in the final collision between the Eastern and Western blocks at ~1.85 Ga that completed the cratonic consolidation (Zhao et al., 2005; 2012; Zhang et al., 2012; 2015). The Archean basement of the Longgang Block is dominated by 2.6–2.5 Ga TTG gneisses with minor supracrustal sequences. Previous metamorphic studies on the Longgang Block have primarily focused on granulite terranes, revealing Neoarchean granulite-facies metamorphism characterized by counterclockwise P–T paths (Zhao et al., 1998; Kwan et al., 2016), with some granulites reaching UHT metamorphic conditions (Duan et al., 2017; Yang and Wei, 2017a; Liu et al., 2022). These counterclockwise P–T paths have been attributed to mantle plume activity (Zhao, 2014) or interpreted as reflecting an Archean-specific vertical tectonic regime (Liu et al., 2024). In contrast, amphibolite-facies supracrustal rocks in the Longgang Block remain understudied, with divergent interpretations regarding their P–T path styles (counterclockwise vs. clockwise) (Zhao et al., 1998; Wu et al., 2013; Liu et al., 2020). The eastern Hebei terrane, located in the northwestern part of the Longgang Block within the North China Craton, extensively exposes Archean crystalline basement composed predominantly of TTG gneisses, K-rich granites, metamorphosed supracrustal rocks, and minor metamorphosed mafic-ultramafic rocks (Wu et al., 1998; Geng et al., 2006; Yang et al., 2008; Nutman et al., 2011; Duan et al., 2017; Liu et al., 2024). Recent systematic studies on metamorphism of TTG gneisses and supracrustal rocks within domal structures in the eastern Hebei region have achieved substantial progress, including: (1) identification of two phases of metamorphism (Neoarchean and Paleoproterozoic), with Paleoproterozoic high-pressure granulite-facies metamorphism displaying clockwise P–T paths that may represent an independent collisional orogeny (Duan et al., 2015; 2019; Yang and Wei, 2017b; Lu and Wei, 2020; Wei et al., 2023); (2) recognition of Neoarchean UHT metamorphism characterized by counterclockwise P–T path involving the prograde process dominated by pressure increase, the UHT peak stage and the post-peak cooling process (Yang and Wei, 2017a; Liu et al., 2022; Zhang et al., 2024); (3) documentation of Neoarchean amphibolite-facies metamorphism with clockwise P–T paths (Liu et al., 2020), explained through sagduction models to account for coexisting diverse metamorphic P–T paths within the same region (Yu et al., 2022; Liu et al., 2024); and (4) discovery of high-pressure to ultrahigh-pressure metamorphism in Neoarchean mafic-ultramafic rocks, interpreted as products of plate tectonic processes (Liu et al., 2018; Wu et al., 2022; Ning et al., 2022; 2023). Nevertheless, metamorphic investigations remain scarce for the Lulong-Shuangshanzi supracrustal belt (Figure 1b). In this paper, systematic data of petrography, mineral chemistry, phase equilibrium modelling and zircon dating are presented for biotite-plagioclase gneisses

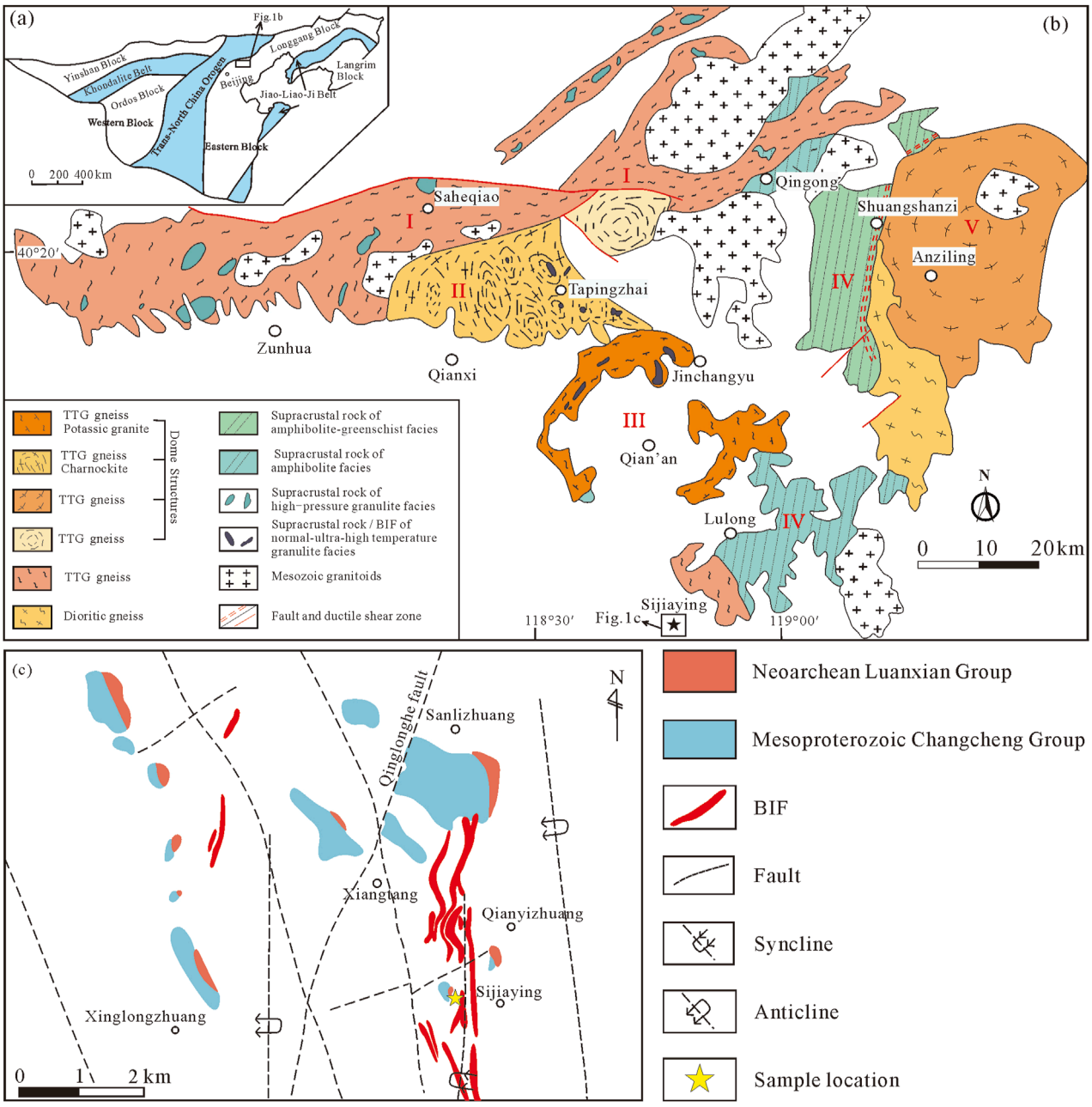

FIGURE 1
(a) The tectonic framework of North China Craton (modified after Zhao et al., 2012). **(b)** Geological map of the East Hebei (modified after Wu et al., 1998; Geng et al., 2006). **(c)** Schematic geological map of the Sijiaying iron ore area showing the distribution of Luanxian Group as well as sample localities (modified after Wu et al., 2015).

from Sijiaying iron deposit area in the eastern Hebei terrane (Figure 1c).

This study aims to (i) evaluate the phase equilibria and P–T evolution for pelitic gneisses from the Luanxian Group; (ii) to constrain the depositional age of biotite-plagioclase gneisses; and (iii) to provide insights into the Neoarchean tectonic setting of the eastern Hebei terrane.

2 Geological setting

The eastern Hebei terrane is characterized by widespread outcrop of early Precambrian basement rocks and preserves the Archean "dome-and-keel" structure (Geng et al., 2006; Duan et al., 2017; Zhao et al., 2021; Liu et al., 2024; Wang et al., 2025). The metamorphic basement complex is predominantly composed

of TTG gneisses, charnockites, potassic granites, (ultra) mafic to felsic supracrustal rocks, and banded iron formations (BIFs) (Sun et al., 2010; Zhao and Zhai, 2013; Guo et al., 2015; Kwan et al., 2016; Liu and Wei, 2018; Fu et al., 2021; Zhang et al., 2024; Zhao et al., 2025). The metamorphic basement of the eastern Hebei terrane can be subdivided into five lithotectonic units (Figure 1b), including (I) the Saheqiao linear tectonic belt, (II) the Taipingzhai gneiss dome, (III) the Qian'an gneiss dome, (IV) the Lulong-Shuangshanzi supracrustal belt, and (V) the Anziling gneiss dome (Wu et al., 1998; Geng et al., 2006). Saheqiao linear tectonic belt exhibits a NEE–EW-trending structural fabric, extending across the Malanyu–Saheqiao–Shangying–Bancheng areas. This belt is primarily composed of TTG gneisses and supracrustal sequences, with the latter predominantly occurring as raft-like enclaves within plutonic intrusions. Zircon U–Pb geochronology constrains the TTG gneisses to magmatic emplacement at 2.55–2.50 Ga, followed by metamorphic overprinting during 2.47–2.31 Ga (Geng et al., 2006; Nutman et al., 2011; Guo et al., 2013; Bai et al., 2014), while minor intrusive bodies yield crystallization ages of ~2.9 Ga (Liou et al., 2017). The supracrustal rafts comprise mafic granulites, amphibolites, ultramafic rocks, pelitic rocks and BIFs, with their protolith formation at ~2.50 Ga and two phases of high-grade metamorphism at 2.51–2.48 Ga and 1.83–1.77 Ga (Zhang et al., 2012; Yang and Wei, 2017b; Lu and Wei, 2020; Liu et al., 2022). Recent studies propose that ultramafic rocks and some garnet clinopyroxenites record high- to ultrahigh-pressure eclogite-facies metamorphism, interpreted as an evidence for Neoarchean plate tectonic regimes involving deep subduction and/or collision processes (Kusky et al., 2022; Ning et al., 2022; 2023; Wu et al., 2022; 2024). However, Zou et al. (2022) recalculated the metamorphic P–T conditions of garnet pyroxenites through revised phase equilibrium modelling, demonstrating that the peak pressure of garnet pyroxenites were overestimated by 7–11 kbar, which should be high-pressure granulite-facies. The gneiss domes are dominated by TTG gneisses, charnockites, potassic granites and supracrustal enclaves. Zircon U–Pb geochronology constrains the magmatic emplacement of TTG gneisses and charnockites to be 2.56–2.48 Ga (Bai et al., 2015; Zhang et al., 2024) with a few of 3.8–2.9 Ga (Nutman et al., 2011; 2014; Liu et al., 2013; Wan et al., 2015; Sun et al., 2016; Chu et al., 2016; Dong et al., 2024; Zhao et al., 2025). The supracrustal rocks from Taipingzhai and the northwestern margin of the Qian'an gneiss dome consists predominantly pelitic granulites, mafic granulites and BIFs, which underwent (UHT) granulite-facies metamorphism with a counterclockwise P–T path during 2.53–2.47 Ga (Kwan et al., 2016; Duan et al., 2017; Liu and Wei, 2020; Liu et al., 2022). The garnet biotite-plagioclase gneisses and fuchsite quartzites from the Caozhuang area underwent amphibolite facies metamorphism with a clockwise P–T path (Liu et al., 2020; 2024). The coexisting diverse P–T–t paths could be well interpreted with a sagduction process (Liu et al., 2024; Yu et al., 2022).

The Lulong–Shuangshanzi supracrustal belt extends north–south between gneiss domes, comprising the Shuangshanzi Group and the Luanxian Group (Sun et al., 2010; Liu et al., 2014). The Shuangshanzi supracrustal rocks consist mainly of greenschist- to amphibolite-facies metavolcanic-sedimentary sequences. Volcanic interlayers record magmatic ages of 2.60–2.51 Ga, overprinted by thermal events at 2.46–2.44 Ga, potentially formed in an island arc (Sun et al., 2010; Guo et al., 2015) or intracontinental rift setting (Zhai, 2011; Lv et al., 2012). The Luanxian Group comprises biotite schist, amphibolites, biotite-plagioclase gneiss, garnet-biotite gneisses, fuchsite quartzites and BIFs (Geng et al., 2006; Chu et al., 2016). The metamorphic volcanic-sedimentary sequences and granitoids in the Lulong area were formed at 2.53–2.50 Ga and 2.51–2.47 Ga, respectively, with anatexis and regional metamorphism occurring between 2.51 and 2.48 Ga (Wang et al., 2019). Wan et al. (2021) redefined the ancient supracrustal rocks exposed in the Labashan and Huangbaiyu areas as the Caozhuang-Labashan supracrustal sequence, which formed at 3.4–3.1 Ga (Zhao et al., 2023) and likely represents a tectonic environment involving mantle plume-crust interaction (Wan et al., 2021; Dong et al., 2024).

3 Analytical methods

This study focuses on detailed petrological investigations, electron probe microanalysis (EPMA), phase equilibria modelling, and zircon U–Pb isotopic geochronology of biotite-plagioclase gneisses (samples N16-1 and N16-6). Analytical work was conducted by Wuhan SampleSolution Analytical Technology Co., Ltd.

3.1 Mineral major element chemistry analysis

The quantitative analysis of *in situ* major elements of minerals was completed by using an electron probe microanalyzer at Wuhan SampleSolution Analytical Technology Co., Ltd., Wuhan, China. Complete the analysis using JXA-8230 of JEOL. The voltage and current analyzed are 15 KV and 10 nA, respectively, with a beam diameter set to 3 μm for feldspar and mica and 1 μm for epidote. The calibration standard samples for the content of major elements use 53 kinds of mineral standard samples, 44 kinds of elemental standard samples, and 15 kinds of rare earth element standard samples provided by SPI Company. The data correction method adopts the ZAF correction method of JEOL. The results are listed in Supplementary Table S1.

3.2 Whole rock major element analysis

The sample pretreatment of whole rock for major element analysis was made by the melting method. The flux is a mixture of lithium tetraborate, lithium metaborate, and lithium fluoride (45:10:5). Ammonium nitrate and lithium bromide were used as oxidants and release agents, respectively. The melting temperature was 1,050°C and the melting time was 15 min. Zsx Primus II wavelength dispersive X-ray fluorescence spectrometer (XRF) produced by RIGAKU, Japan was used for the analysis of major elements in the whole rock. The data were corrected by the theoretical α coefficient method. The relative standard deviation (RSD) is less than 2%. The whole-rock geochemical data are presented in Table 1.

TABLE 1 Bulk-rock compositions of supracrustal rocks from Luanxian Group.

XRF whole rock composition (wt.%)													
Sample	SiO_2	TiO_2	Al_2O_3	$Fe_2O_3^T$	MnO	MgO	CaO	Na_2O	K_2O	P_2O_5	LOI	Mg#	A/CNK
N12-6	43.43	0.50	16.12	19.76	0.24	6.22	3.49	0.74	6.91	0.24	1.59	0.26	1.45
N12-7	65.89	0.36	14.8	4.44	0.06	2.69	1.39	4.81	3.52	0.15	1.28	0.40	1.53
N16-1	67.02	0.42	12.73	5.95	0.07	2.91	2.56	3.38	2.63	0.13	1.45	0.35	1.48
N16-2	66.33	0.40	14.42	4.88	0.06	2.60	2.04	5.10	2.33	0.13	1.14	0.37	1.52
N16-6	67.45	0.36	14.04	4.34	0.05	2.19	1.70	4.01	3.48	0.12	1.54	0.36	1.53
Normalized molar proportion used for phase equilibria modelling (mole %)													
Sample	Figure	H_2O	Na_2O	MgO	Al_2O_3	SiO_2	K_2O	CaO	FeO	TiO_2	MnO	O_2	
N16-1	Figure 4	9.76	2.94	4.47	7.56	66.38	1.95	2.33	4.14	0.32	0.00	0.15	
N16-6	Figure 5	9.90	3.71	3.17	8.65	67.02	2.42	1.55	3.13	0.24	0.10	0.10	

3.3 Zircon U–Pb analysis

U–Pb dating and trace element analysis of zircon were simultaneously conducted by LA-ICP-MS at the Wuhan SampleSolution Analytical Technology Co., Ltd., Wuhan, China. An Agilent 7900 ICP-MS instrument was used to acquire ion-signal intensities. The spot size and frequency of the laser were set to 24 μm and 5Hz, respectively. Zircon Tanz and glass NIST610 served as external standards for U–Pb dating and trace element calibration (Hu et al., 2021), respectively. Each analysis incorporated a background acquisition of approximately 20–30 s, followed by 50 s of data acquisition from the sample. An Excel-based software, ICPMSDataCal, was used to perform off-line selection and integration of background and analyzed signals, time-drift correction, and quantitative calibration for trace element analysis and U–Pb dating (Liu et al., 2008). Concordia diagrams and weighted mean calculations were conducted using Isoplot/Ex_ver3 (Ludwig, 2003). The results are listed in Supplementary Table S2.

4 Results

4.1 Field characteristics of samples

The investigated suite comprises biotite-plagioclase gneisses and biotite schist sampled from the Sijiaying iron ore district, Xiangtang Town, Luanzhou City. These supracrustal units are stratigraphically interlayered with BIFs, which exhibit characteristic rhythmic alternations of siliceous and iron-rich laminae (Figure 2a). Within the biotite schist, a penetrative tectonic foliation is defined by preferentially oriented biotite aggregates, displaying continuous planar alignment wherein quartz, plagioclase, and K-feldspar form elongate grains parallel to the foliation plane (Figure 2b). Sample N16-1 (biotite-plagioclase gneiss) manifests typical gneissic banding with irregular lenticular segregations of biotite-dominated mafic layers contrasting against felsic mineral domains (Figure 2c). While sharing similar structural characteristics, sample N16-6 exhibits coarser-grained gneissose banding relative to N16-1 (Figure 2d).

4.2 Petrography and chemistry

The main mineral components in biotite schist (N12-6) include biotite (65 vol%), K-feldspar (14%), plagioclase (3%), epidote (8%), and quartz (10%), with minor accessory minerals such as zircon and apatite (Figure 2e). The K-feldspar grains are uniformly sized (0.1–0.2 mm), appearing subhedral to anhedral. Chemically, the K-feldspars are dominated by microcline (Figure 3a). Biotite can be divided into two types based on grain size. The coarse-grained biotite is of 0.4–0.7 mm across, and the fine-grained one is 0.1–0.3 mm across (Figure 2h). Chemical composition analysis reveals that the X_{Mg} [= $Mg/(Fe^{2+} + Mg)$] of biotite shows limited variation (0.39–0.41). The X_{Ti} content in fine-grained biotite (0.03–0.05 a.p.f.u.) is slightly lower than those in coarse-grained biotite (0.04–0.07 a.p.f.u.) (Figure 3b). Both types are classified as ferroan biotite based on their compositional plots (Figure 3c). Epidote occurs either as cross-cutting veins through biotite or as disseminated grains within the matrix.

The biotite-plagioclase gneiss (N16-1) exhibits a grayish-black color with gneissic structure characterized by oriented biotite flakes intergrown with granular minerals (Figure 2f). The mineral assemblage comprises biotite (25 vol%), K-feldspar (2%), plagioclase (34%), epidote (3%), and quartz (36%), along with accessory muscovite, sphene, zircon and calcite (Figure 2i). Biotite grains show uniform size. Microprobe traverses of biotite exhibit zoning profiles, with the X_{Ti} contents increasing from core to rim (0.085–0.102), while X_{Mg} values (0.52–0.53) in biotite is homogeneous. According to compositional discrimination diagrams, they were classified as magnesian biotite (Figure 3c). K-feldspar occurs as xenomorphic to subhedral microcline, while plagioclase is predominantly

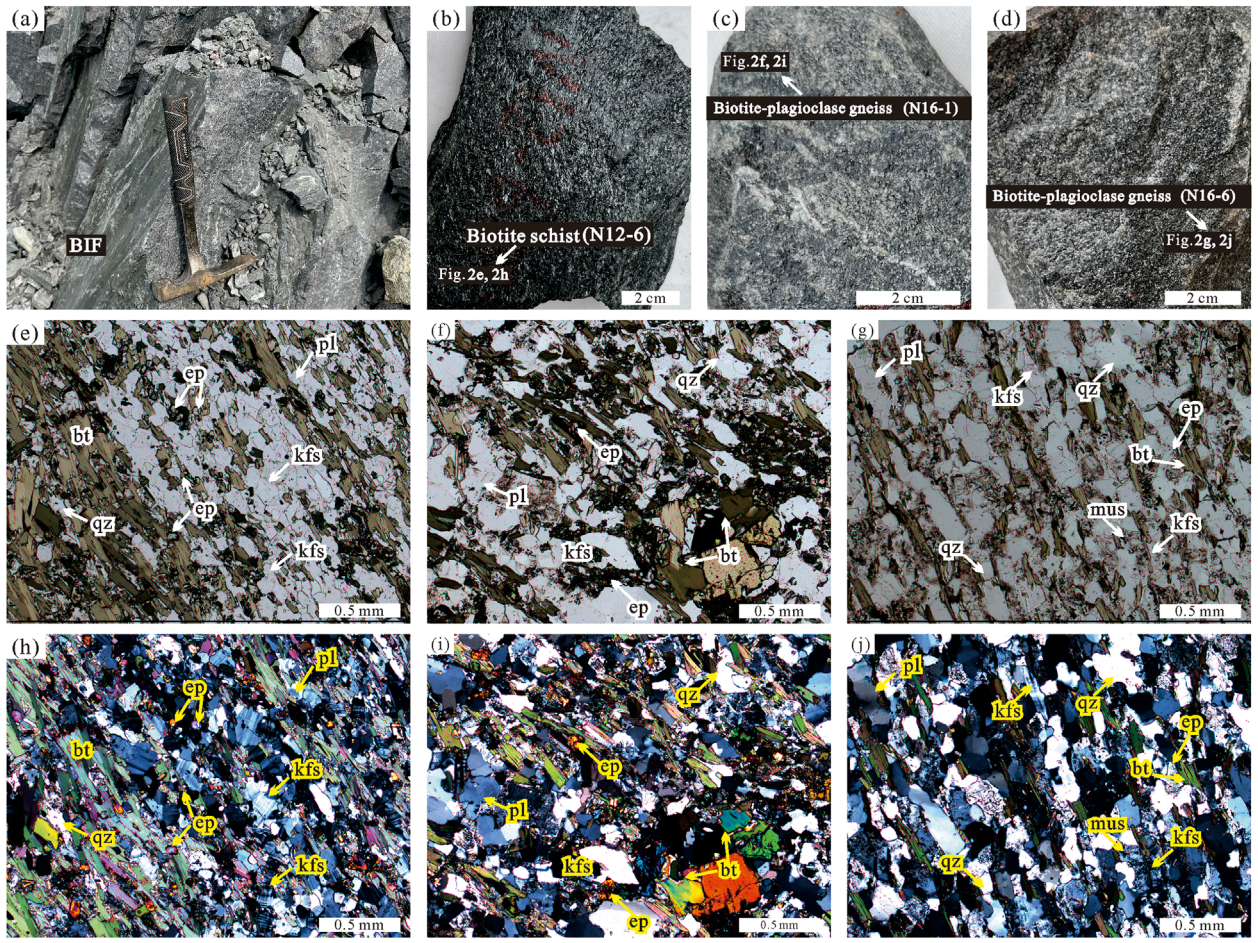

FIGURE 2
Field photographs and photomicrographs of the supracrustal rocks in Sijiaying. **(a–d)** Outcrop Photographs of supracrustal rocks and BIFs. **(e–g)** Photomicrographs of biotite schist and biotite-plagioclase gneisses showing the mineral assemblages in samples N12-6, N16-1 and N16-6. Plane polarized light. **(h–j)** Photomicrographs of biotite schist and biotite-plagioclase gneisses showing the mineral assemblages in samples N12-6, N16-1 and N16-6. Crossed polarized light. Abbreviations of minerals: bt, biotite; ep, epidote; pl, plagioclase; kfs, K-feldspar; qz, quartz; mus, muscovite.

oligoclase with X_{An} = 0.20–0.21. Some albite grains occur as inclusions in biotite. Epidote occurs as fine-grained aggregates in the matrix.

The mineral assemblage in sample N16-6 consists mainly of biotite (18 vol%), K-feldspar (9%), plagioclase (43%), muscovite (1%), and quartz (29%), along with minor epidote, albite and zircon (Figure 2g). The biotite can be divided into coarse-grained biotite (0.3–0.4 mm) and fine-grained biotite (<0.2 mm) based on grain size (Figure 2j). The X_{Ti} contents in coarse-grained biotite generally decrease (0.104–0.088) from core to rim, while X_{Ti} contents in fine-grained biotite is relatively homogeneous (0.099–0.090). Both types exhibit X_{Mg} values of 0.49–0.51, indicating magnesian biotite based on compositional classification diagrams (Figure 3c). The K-feldspar has a grain size of 0.2–0.3 mm, all being microcline. Plagioclase grains are across of 0.2–0.5 mm, being oligoclase with X_{An} = 0.17–0.23. Minor fine-grained epidote and albite occurs as inclusions within biotite grains, interpreted to have formed in a later stage than the matrix biotite.

The representative supracrustal rock samples collected from Sijiaying area include biotite schist and biotite-plagioclase gneisses. The biotite schist (N12-6) has a SiO_2 content of 43.43 wt%, which is lower than that of the biotite-plagioclase gneisses. It exhibits higher Al_2O_3 (16.12 wt.%) and $Fe_2O_3^T$ (19.76 wt.%), with MgO = 6.22 wt.%, CaO = 3.49 wt.%, X_{Mg} = 0.26, and A/CNK = 1.45 (Table 1). Combined with protolith reconstruction diagrams, these data indicate that the protolith of this schist is shale formed in an Fe-Al-rich sedimentary environment (Figure 3d). The biotite-plagioclase gneisses have SiO_2 contents of 65.89–67.45 wt.%, Al_2O_3 = 12.73–14.89 wt.%, $Fe_2O_3^T$ = 4.34–5.95 wt.%, MgO = 2.19–2.91 wt.%, CaO = 1.39–2.56 wt.%, X_{Mg} = 0.35–0.40, and A/CNK = 1.48–1.53. The protoliths of these gneisses are classified as greywacke on the discrimination diagram (Figure 3d).

4.3 Zircon U–Pb age

The zircon grains in sample N16-1 are predominantly subhedral to anhedral, displaying prismatic or elliptical shapes (Figure 4a), with aspect ratios of 1:1–1:3 and long-axis lengths of 50–130 μm.

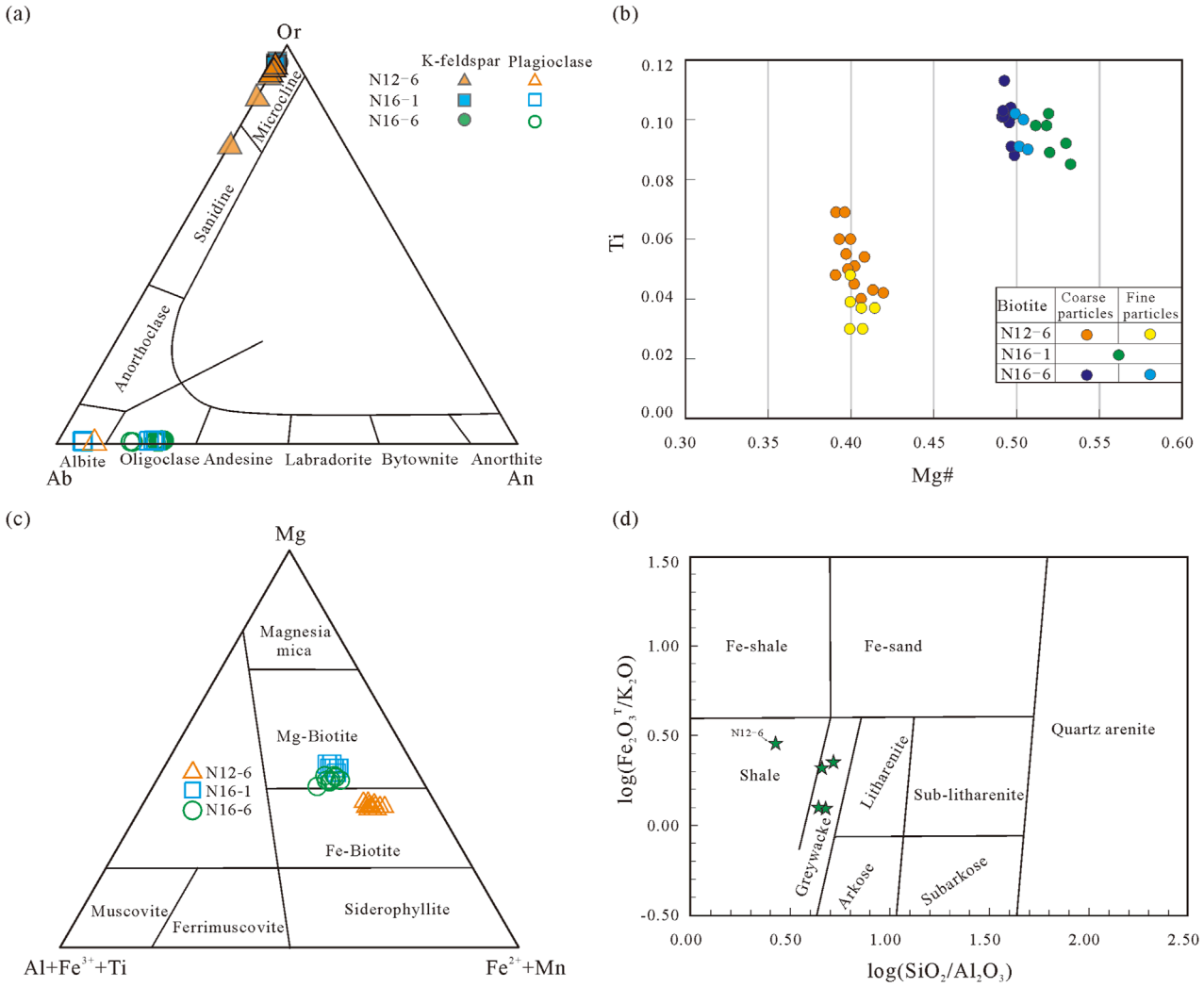

FIGURE 3
(a) An–Ab–Or diagram showing the compositions of ternary feldspars (after Aldahaan, 2020). **(b)** Ti–X_{Mg} diagram for biotite. **(c)** Mg–Al + Fe^{3+}+Ti–Fe^{2+}+Mn diagram showing the classification of biotite (after Foster, 1960). **(d)** Protolith discrimination diagrams for supracrustal Rocks (after Herron, 1988).

Most zircons exhibit core-rim structures, where the cores show distinct or blurred oscillatory zoning, suggesting their magmatic orogin (Wu and Zheng, 2004). While a few displays planar zoning or without zoning. The rims are extremely narrow and dark gray. A total of 70 analytical spots on 62 zircon grains were analyzed for trace element compositions and U–Pb dating. The Th/U ratios range from 0.05 to 1.23. In the $^{207}Pb/^{235}U$-$^{206}Pb/^{238}U$ concordia diagram (Figure 4c), most zircons deviate from the concordia line due to varying degrees of Pb loss. The $^{207}Pb/^{206}Pb$ apparent ages range from 1731 ± 55 Ma to 2,898 ± 59 Ma, with a peak age of 2,552 Ma. Analyses plotting on or near the concordia line yield a weighted mean $^{207}Pb/^{206}Pb$ age of 2,547 ± 14 Ma (MSWD = 0.32, n = 29).

The zircon grains in sample N16-6 are predominantly subhedral to anhedral, displaying prismatic or elliptical shapes (Figure 4b), with aspect ratios of 1:1–1:2 and sizes of 60–120 μm. Most zircons exhibit core-rim structures, where the cores show distinct or blurred oscillatory zoning, while a few displays weak planar zoning with bright luminescence. The rims are extremely narrow and light gray. A total of 73 analytical spots on 64 zircon grains were analyzed for trace element compositions and U–Pb dating. The Th/U ratios range from 0.18 to 1.61. In the $^{207}Pb/^{235}U$-$^{206}Pb/^{238}U$ concordia diagram (Figure 4d), most zircons deviate from the concordia line due to varying degrees of Pb loss. The $^{207}Pb/^{206}Pb$ apparent ages range from 2,229 ± 67 Ma to 2,727 ± 37 Ma, with a peak age of 2,556 Ma. Analyses plotting on or near the concordia line yield a weighted mean $^{207}Pb/^{206}Pb$ age of 2,555 ± 14 Ma (MSWD = 0.30, n = 41). Chondrite-normalized REE patterns show that zircon grains from samples N16-1 and N16-6 predominantly display positive Ce anomalies, $(Lu/Gd)_N$ values of 2.22–89.86, and HREE contents higher than LREE, resulting in steeply left-inclined patterns (Figures 4e,f).

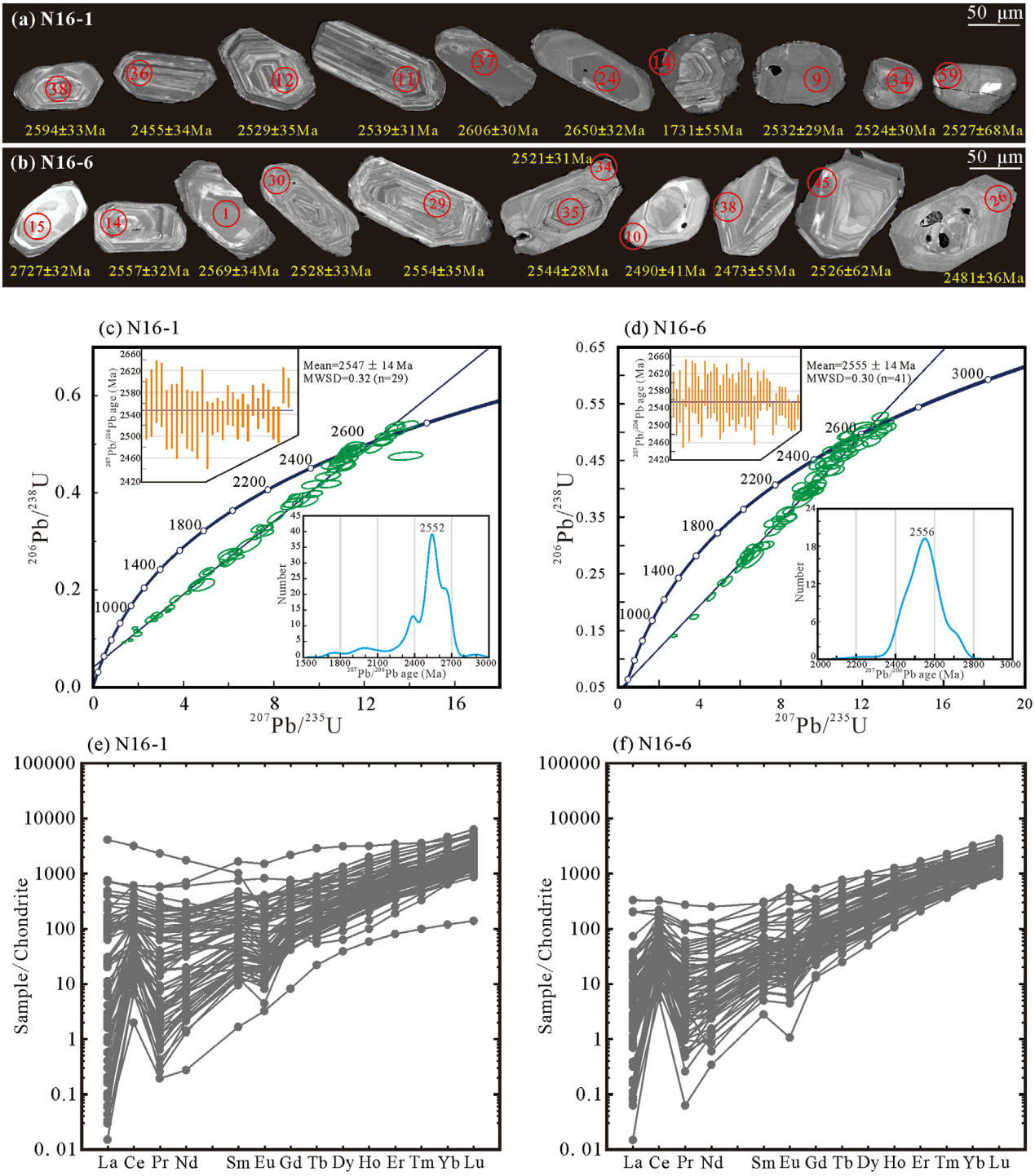

FIGURE 4
(a,b) Cathodoluminescence images of representative zircon grains from samples N16-1 and N16-6, showing the inner structures, analyzed U–Pb locations, and calculated apparent $^{207}Pb/^{206}Pb$ ages. **(c,d)** Zircon U–Pb isotopic concordia diagrams of samples N16-1 and N16-6. **(e,f)** Chondrite normalized REE patterns of zircon grains (Sun and McDonough, 1989).

4.4 Phase equilibria modelling

Phase quilibria are modelled for samples N16-1 and N16-6 in the system MnNCKFMASHTO (MnO-Na_2O-CaO-K_2O-FeO-MgO-Al_2O_3-SiO_2-H_2O-TiO_2-O). Calculations are performed using GeoPs software (Xiang and Connolly, 2021) incorporating the ds62 thermodynamic dataset (Holland and Powell, 2011). Mineral and activity-composition models used in the calculations are plagioclase and K-feldspar (Holland and Powell, 2003), biotite and muscovite (White et al., 2014), epidote (Holland and Powell, 1998), ilmenite

and magnetite (White, 2000), garnet, chlorite, cordierite and melt (White et al., 2014). Sillimanite, andalusite, rutile, titanite, and quartz were pure end-member components. P–T pseudosection for each sample was calculated using an effective bulk-rock composition which was generated according to mass balance constraints by integrating mineral compositions and modal abundance data of the phases present (Carson et al., 1999). The effective bulk-rock compositions used for phase diagram calculations are listed in Table 1.

4.4.1 Sample N16-1

The P–T pseudosection for sample N16-1 was constructed over a range of 1–8 kbar/400°C–800°C (Figure 5). Biotite and quartz are present in all mineral assemblages. The water-saturated solidus in this pseudosection occurs at 655°C–735°C, showing a steep negative slope, with a gentler slope at pressures <2.6 kbar. The disappearance line of K-feldspar nearly coincides with the solidus. The peak mineral assemblage (bt + kf + pl + qz + ep + mus + sph + H_2O) is stable at 4.5–10 kbar/520°C–620°C. The pseudosection is contoured with isopleths of X_{Ti} and X_{Mg} [= Mg/(Mg + Fe^{2+})] in biotite, and X_{An} in plagioclase. The X_{Ti} isopleths of biotite display steep slopes and increases with rising temperature within the rutile-bearing and/or sphene-bearing assemblage. The X_{Mg} isopleths of biotite display positive slopes. The X_{An} isopleths increases with the pressure decreasing. The measured minimum X_{An} of 0.20 from the core of matrix plagioclase, the maximum X_{Ti} of 0.102 together with X_{Mg} of 0.53 from the matrix biotite define a peak P–T condition of ~7.4 kbar/586°C. Combine with the increasing X_{Ti} from core to rim in matrix biotite, a prograde path with P–T condition increasing during the pre-peak process was predicted.

4.4.2 Sample N16-6

The P–T pseudosection for sample N16-6 was constructed over a range of 1–10 kbar/400°C–800°C (Figure 6). Biotite is stable throughout the calculated P–T range. The water-saturated solidus occurs at 635°C–730°C, showing a steep negative slope at pressures >3 kbar and a gentler slope at pressures <3 kbar. The peak mineral assemblage (bt + kfs + pl + mus + qz + H_2O) is stable at 1.7–8.4 kbar/587°C–663°C. Mineral composition isopleths plotted in the pseudosection include X_{Ti} and $Fe^{2+}/3$ in biotite, and X_{An} in plagioclase. The X_{An} isopleths of plagioclase exhibit steep positive slopes at temperatures below ~550°C and above ~640°C, while showing gentler slopes between 550°C and 640°C, with X_{An} values gradually increasing as pressure decrease. The X_{Ti} isopleths of biotite generally display steep slopes in rutile-bearing and garnet-bearing mineral assemblages. X_{Ti} content increases with rising temperature in ilmenite-bearing and rutile-bearing assemblages. The measured minimum X_{An} of 0.17 from the matrix plagioclase, the maximum X_{Ti} of 0.104 together with X_{ann} of 0.417 from the core of the coarse-grained biotite define a peak P–T condition of ~7.0 kbar/630°C. The increasing X_{An} in plagioclase from core to rim (0.17–0.23) and the decreasing X_{Ti} in coarse-grained biotite constrain a post-peak decompression and cooling process. The pre-peak process is characterized by the epidote and albite inclusion assemblage in matrix biotite and feldspar. Therefore, a clockwise P–T path is constrained.

5 Discussion

5.1 Metamorphic evolution of supracrustal rocks

Based on the petrographic characteristics and phase equilibria modelling, the metamorphic evolution of the supracrustal rocks from Sijiaying area, eastern Hebei, includes three stages: (i) pre-peak prograde to peak stage; (ii) peak stage; and (iii) post-peak decompression and cooling stage. For sample N16-6, a clockwise P–T path involving peak condition and post peak decompression and cooling process was well defined. The peak P–T condition was constrained to be at ~7.0 kbar/630°C based on the minimum X_{An} in plagioclase and maximum X_{Ti} isopleths in biotite, followed by decompression and cooling with metamorphic reaction of pl + mus = bt + kfs + qz + H_2O. The pre-peak prograde process can be inferred from the inclusion assemblages of epidote, sphene and albite within biotite and K-feldspar, which was dominated by metamorphic reaction of mus + ab + ep + sph + qz = kfs + bt + pl + H_2O. For sample N16-1, the pre-peak prograde to peak stage is inferred on the basis of biotite zoning and inclusions in matrix biotite and feldspar, showing a P–T segment with increase in both pressure and temperature, dominated by metamorphic reaction of ab + sph + ep + mus + qz = Pl + bt + kfs + H_2O. The peak condition is defined by the minimum X_{An} in plagioclase and maximum X_{Ti} isopleths in biotite. The post-peak stage, including decompression process, in sample N16-1 is inferred to be similar as those in sample N16-6. Phase equilibria modelling for sample N12-6 (biotite schist) defines broadly constrained P–T conditions, precluding precise determination of peak metamorphism. However, the X_{Ti} in biotite (0.03–0.07 a.p.f.u.) from biotite schist is markedly lower than that of the two biotite-plagioclase gneiss samples, suggesting greenschist-facies metamorphism indicative of shallower crustal depths relative to the gneissic units.

5.2 Timing of deposition

Previous geochronological studies on the eastern Hebei terrane demonstrate that the protolith of metamorphic supracrustal rocks predominantly formed between 2.61 and 2.50 Ga (Guo et al., 2013; Wan et al., 2015; Sun et al., 2016; Fu et al., 2016; Lu et al., 2017; Duan et al., 2017; Liu and Wei, 2020), with magmatic activity concentrated at 2.56–2.48 Ga (Geng et al., 2006; Nutman et al., 2011; Bai et al., 2016; Yang and Wei, 2017b; Li et al., 2019; Duan et al., 2022). The eastern Hebei terrane underwent two phases of metamorphism during the Neoarchean and Paleoproterozoic, with metamorphic ages primarily concentrated at 2.53–2.47 Ga and 1.85–1.77 Ga (Geng et al., 2006; Nutman et al., 2011; Yang and Wei, 2017b; Duan et al., 2019; Liu et al., 2020; Li et al., 2024). The biotite-plagioclase gneisses of the Luanxian Group in this study contain magmatic zircon grains with significantly old $^{207}Pb/^{206}Pb$ apparent ages of 2.90–2.63 Ga, indicating the presence of ancient rocks or zircons in the source region. Some ancient age records have also been reported from Labashan area (>3.4 Ga) in Lulong County (Chu et al., 2016; Wan et al., 2021; Zhao et al., 2023; Dong et al., 2024), Zhuzhangzi area (>2.90 Ga) in Qinglong County (Sun et al., 2010; Guo et al., 2015) and Huangbaiyu area in Qian'an

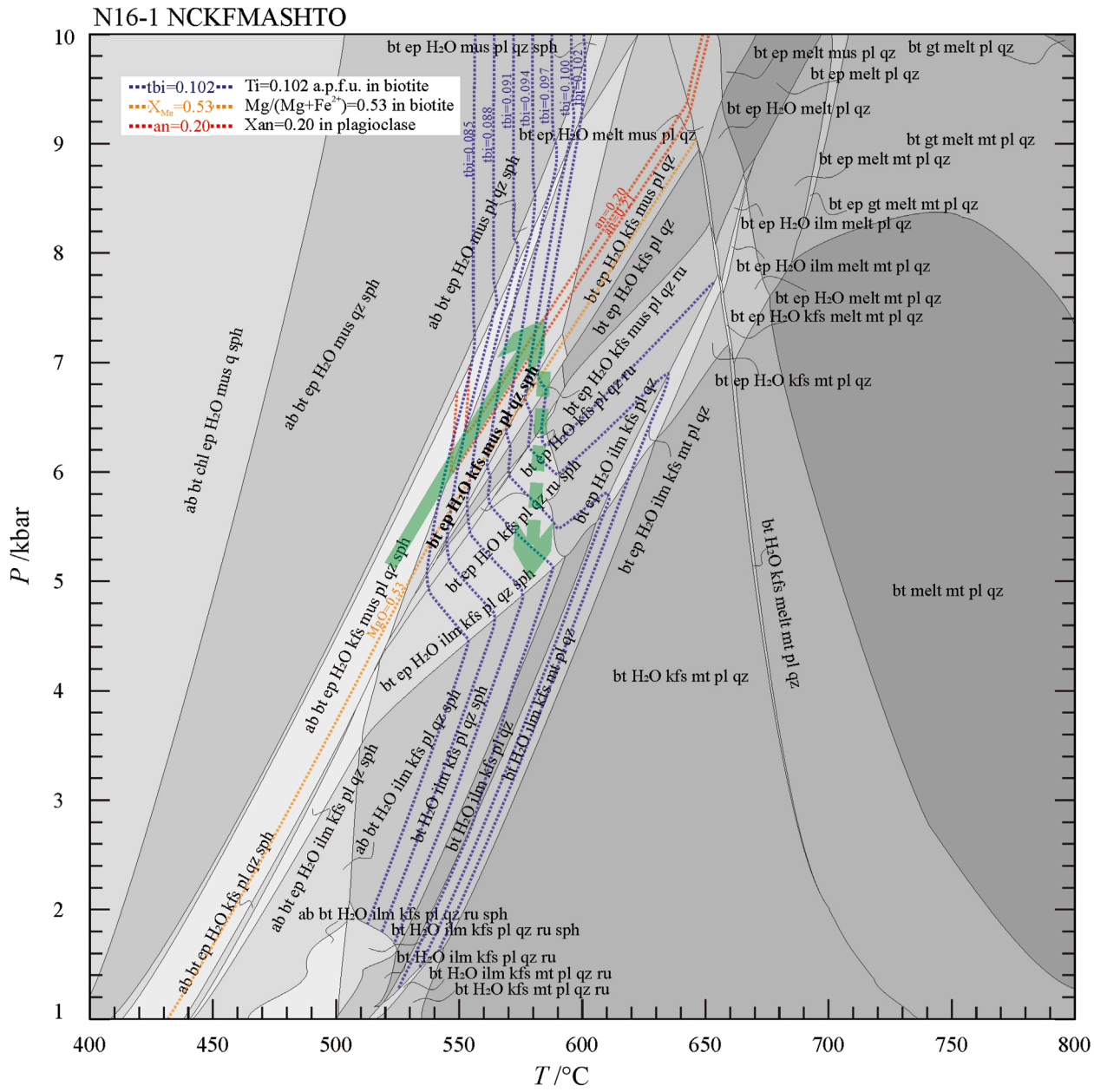

FIGURE 5
P-T pseudosection for sample N16-1 in the systems NCKFMASHTO. The pseudosection is contoured with isopleths of biotite and plagioclase for relevant assemblages. Compositions used for modelling the *P-T* pseudosection are listed in Table 1. Abbreviations of minerals: bt, biotite; ep, epidote; pl, plagioclase; kfs, K-feldspar; qz, quartz; mus, muscovite; gt, garnet; sph, sphene; ab, albite; mt, magnetite; ru, rutile; ilm, ilmenite; and, andalusite; sill, sillimanite; crd, cordierite.

(>3.8 Ga) (Liu et al., 1992; Wu et al., 2005; Wilde et al., 2008), indicating prolonged and widespread Archean magmatism. The youngest concordant $^{207}Pb/^{206}Pb$ age group together with weight mean ages of 2,547 ± 14 Ma and 2,555 ± 14 Ma from biotite-plagioclase gneiss provides a maximum age for the deposition of the Luanxian supracrustal rocks in this study, which is consistent with the depositional age of the Sijiaying BIFs (Cui et al., 2014; Han et al., 2014; Fu et al., 2021; Gao et al., 2023). Metamorphic volcanic rocks and BIFs from the Luanxian Group record ~2.50 Ga metamorphic ages (Han et al., 2014; Gao et al., 2023).

5.3 Tectonic implications

The tectonic evolution of the Precambrian basement in the eastern Hebei terrane during the Neoarchean remains debated. Multiple geodynamic models have been proposed to explain the tectonic setting of Archean metamorphism, including: (1) horizontal tectonic models involving microcontinental block subduction-collision or oceanic slab subduction leading to continent-continent collision (Zhai and Santosh, 2011; Nutman et al., 2011; Fu et al., 2017; Lu et al., 2017; Liu et al., 2018;

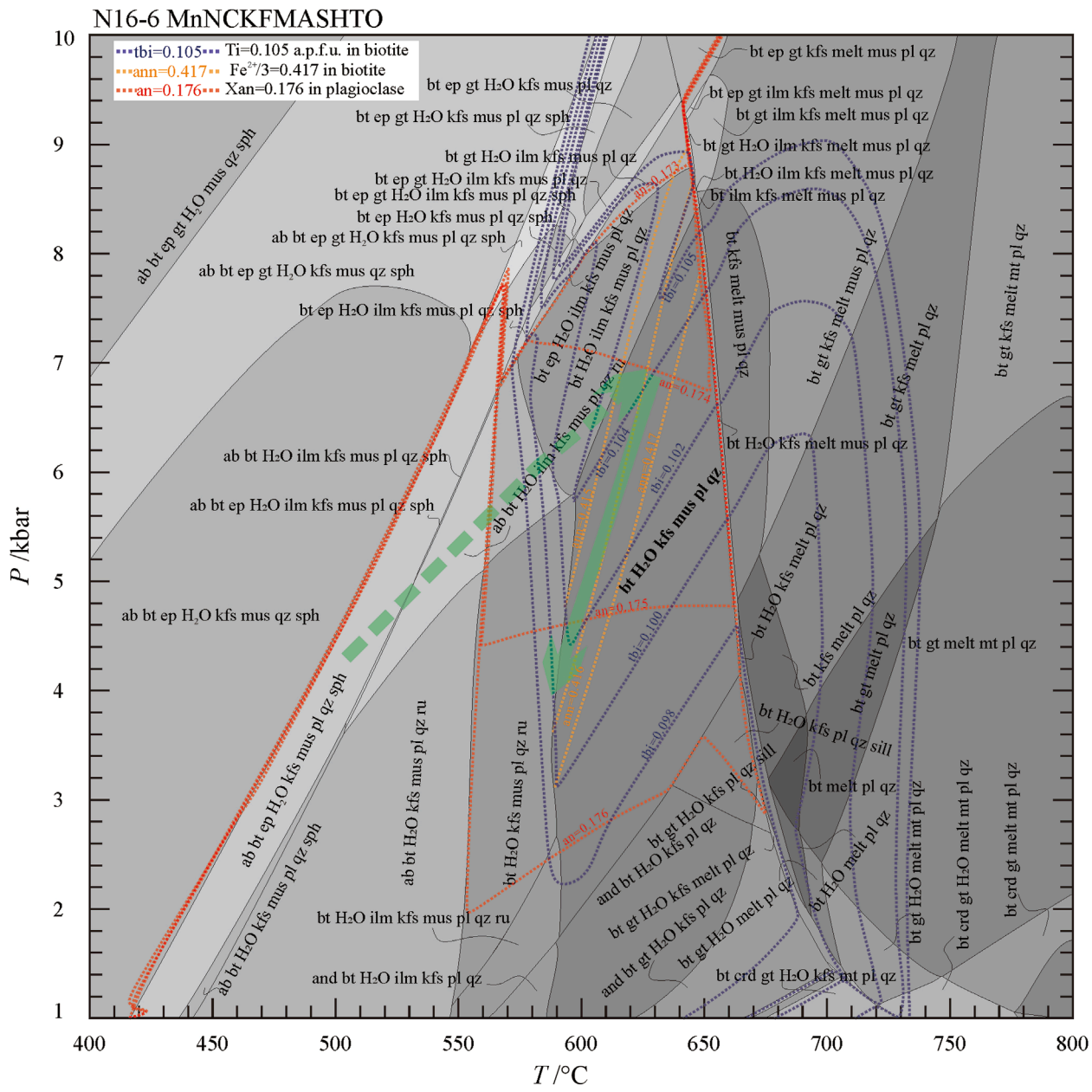

FIGURE 6
P-T pseudosection for sample N16-6 in the systems MnNCKFMASHTO. The pseudosection is contoured with isopleths of biotite and plagioclase for relevant assemblages. Compositions used for modelling the *P-T* pseudosection are listed in Table 1. Abbreviations of minerals are the same as in Figure 5.

Kusky et al., 2022; Ning et al., 2023; Wu et al., 2022); (2) Vertical tectonic models associated with mantle plume activity (Zhao et al., 1998; Geng et al., 2006; Yang et al., 2008; Zhao and Zhai, 2013; Kwan et al., 2016); and (3) Archean-specific vertical tectonic regimes associated with sagduction (Duan et al., 2017; Liu et al., 2024; Yu et al., 2022; Li et al., 2024). By integrating the metamorphic evolution and geochronological results obtained from the Luanxian supracrustal rocks with previous studies, we propose that a sagduction model dominated the Neoarchean tectonic regime of the eastern Hebei terrane, evidenced by: (1) Despite multiple phases of metamorphic and deformational overprinting, the Archean dome-and-keel architecture preserved in the eastern Hebei terrane, which distinctly differs from the linear structural patterns of Phanerozoic orogenic belts (Zhao et al., 1999; 2012; Liu et al., 2018; 2024; Zhao et al., 2021; Yu et al., 2022; Xu et al., 2022); (2) Plutonic intrusions (e.g., TTG gneisses, K-rich granites, and quartz diorites) are widespread and coeval, emplaced within a narrow age range (Geng et al., 2006; Yang et al., 2008; Nutman et al., 2011; Wan et al., 2015); (3) The depositional age of supracrustal protoliths shows approximate temporal coincidence with regional magmatism and metamorphism (Zhao and Zhai, 2013; Wan et al., 2015; Duan et al., 2017; Liu et al., 2020; 2024; Zhao et al., 2021; Chen et al., 2024); (4) The Shuangshanzi-Lulong supracrustal

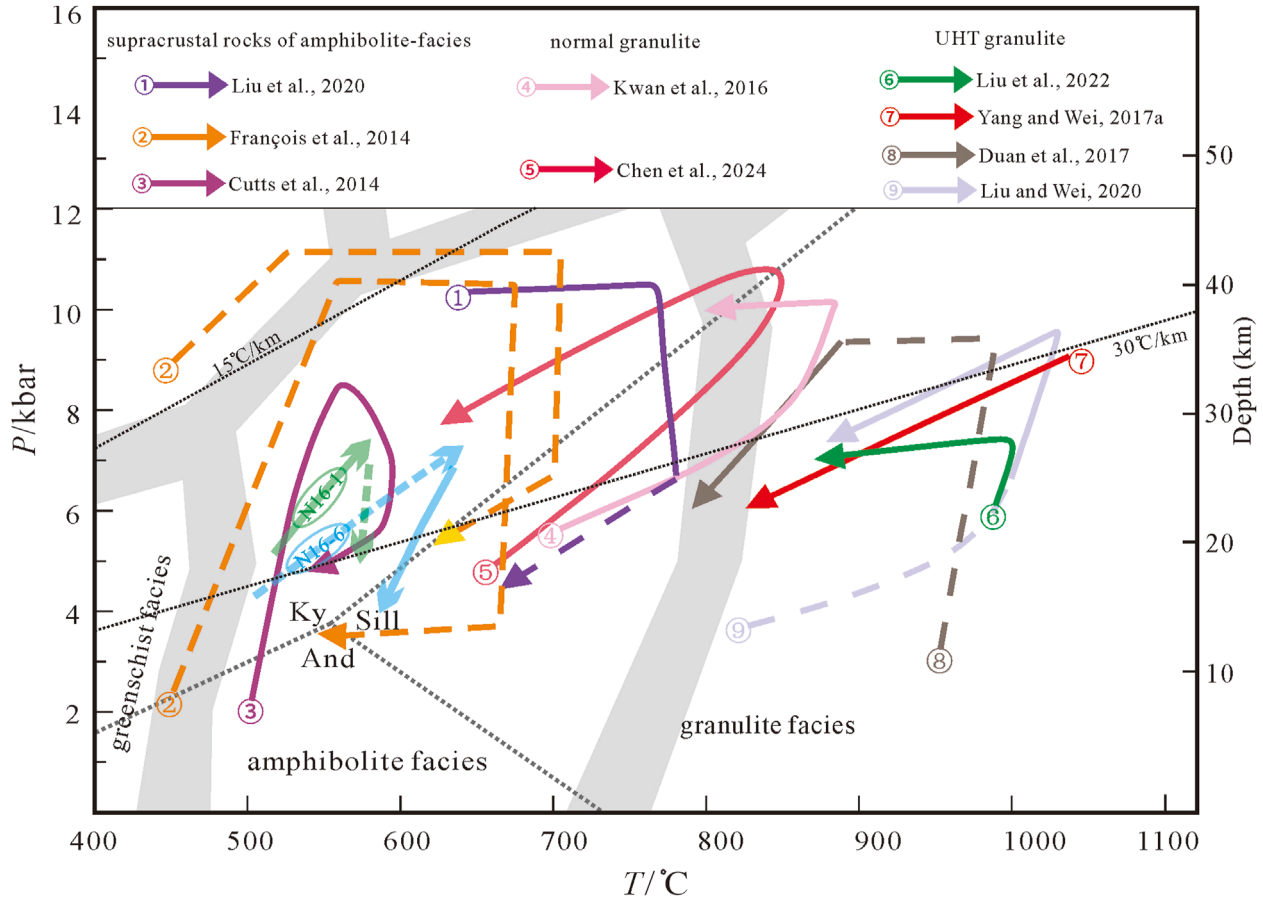

FIGURE 7
The summarized metamorphic *P-T* conditions and paths for supracrustal rocks from the East Hebei terrane and their comparison with those from Stolzburg block and the East Pilbara Terrane. Metamorphic facies boundaries follow the classification by Brown and Johnson (2018).

belt, located within the Qian'an and Anziling gneiss domes, exhibits a synformal structure with subvertical lineations and sinistral ductile shear zones, indicating downward sag relative to TTG gneisses (Liu et al., 2017; Zhao et al., 2021); (5) The Luanxian Group supracrustal rocks underwent amphibolite-facies metamorphism with a clockwise P-T path and a geothermal gradient of 24°C/km, analogous to the evolution of supracrustal sequences in the Pilbara craton (Figure 7) (François et al., 2014; Cutts et al., 2014), which was attributed to sagduction according to numerical simulation results (François et al., 2014; Sizova et al., 2018; Yu et al., 2022; Liu et al., 2024).

6 Conclusion

The geological, mineralogical, zircon U–Pb geochronological data and phase equilibria modelling results of the Luanxian supracrustal rocks in eastern Hebei terrane presented in this study lead to the following conclusions:

(1) Biotite-plagioclase gneisses in the Luanxian Group show clockwise P–T path characteristic of amphibolite-facies metamorphism, comprising pre-peak heating and compression to peak P–T conditions of ~7.0 kbar/630°C and ~7.4 kbar/586°C, followed by post-peak decompression and cooling.

(2) The protoliths of the Luanxian supracrustal rocks, composed of pelitic rocks and greywackes, were deposited at ~2.55 Ga and subsequently underwent regional metamorphism.

(3) The eastern Hebei terrane was dominated by a vertical tectonic regime during the Neoarchean.

Data availability statement

The original contributions presented in the study are included in the article/Supplementary Material, further inquiries can be directed to the corresponding authors.

Author contributions

DZ: Formal Analysis, Writing – original draft, Methodology, Software, Data curation, Investigation. ZD: Writing – original

draft, Funding acquisition, Conceptualization, Supervision, Project administration, Writing – review and editing, Methodology, Data curation, Investigation. WC: Writing – review and editing, Investigation, Methodology, Supervision, Formal Analysis. LY: Software, Methodology, Writing – original draft, Formal Analysis. JL: Writing – original draft, Software, Formal Analysis, Data curation, Methodology. ZT: Formal Analysis, Writing – original draft, Data curation, Methodology. JZ: Supervision, Formal Analysis, Writing – original draft, Methodology.

Funding

The author(s) declare that financial support was received for the research and/or publication of this article. This article was financially supported by the National Natural Science Foundation of China (Grant No. 41902060), the Natural Science Foundation of Hebei Province of China (Grant No. D2024403070), and the PhD Research Startup Foundation of Hebei GEO University (Grant No. BQ2024012).

Acknowledgments

We thank the Editor and the two reviewers for their thoughtful and constructive comments. We thank Tiange Xie for her involvement in the field work.

Conflict of interest

The authors declare that the research was conducted in the absence of any commercial or financial relationships that could be construed as a potential conflict of interest.

Generative AI statement

The author(s) declare that no Generative AI was used in the creation of this manuscript.

Publisher's note

All claims expressed in this article are solely those of the authors and do not necessarily represent those of their affiliated organizations, or those of the publisher, the editors and the reviewers. Any product that may be evaluated in this article, or claim that may be made by its manufacturer, is not guaranteed or endorsed by the publisher.

Supplementary material

The Supplementary Material for this article can be found online at: https://www.frontiersin.org/articles/10.3389/feart.2025.1655963/full#supplementary-material

References

Aldahaan, S. A. M. (2020). *Rock-forming minerals*. Rock-forming minerals.

Bai, X., Liu, S., Guo, R., and Wang, W. (2015). Zircon U–Pb–Hf isotopes and geochemistry of two contrasting Neoarchean charnockitic rock series in eastern Hebei, north China craton: implications for petrogenesis and tectonic setting. *Precambrian Res.* 267, 72–93. doi:10.1016/j.precamres.2015.06.004

Bai, X., Liu, S., Guo, R., and Wang, W. (2016). A Neoarchean arc–back-arc system in eastern Hebei, north China craton: constraints from zircon U–Pb–Hf isotopes and geochemistry of dioritic–tonalitic–trondhjemitic–granodioritic (DTTG) gneisses and felsic paragneisses. *Precambrian Res.* 273, 90–111. doi:10.1016/j.precamres.2015.12.003

Bai, X., Liu, S., Guo, R., Zhang, L., and Wang, W. (2014). Zircon U–Pb–Hf isotopes and geochemistry of neoarchean dioritic–trondhjemitic gneisses, eastern hebei, north China craton: constraints on petrogenesis and tectonic implications. *Precambrian Res.* 251, 1–20. doi:10.1016/j.precamres.2014.05.027

Brown, M., and Johnson, T. (2018). Secular change in metamorphism and the onset of global plate tectonics. *Am. Mineral.* 103, 181–196. doi:10.2138/am-2018-6166

Campbell, I. H., and Hill, R. I. (1988). A two-stage model for the formation of the granite-greenstone terrains of the kalgoorlie-norseman area, western Australia. *Earth Planet. Sci. Lett.* 90, 11–25. doi:10.1016/0012-821X(88)90107-0

Carson, C., Powell, R., and Clarke, G. (1999). Calculated mineral equilibria for eclogites in $CaO–Na_2O–FeO–MgO–Al_2O_3–SiO_2–H_2O$: application to the poue'bo Terrane, Pam Peninsula, New Caledonia. *J. Metamorph. Geol.* 17, 9–24. doi:10.1046/j.1525-1314.1999.00177.x

Chen, Z., Wang, G., Li, T., Zhou, J., Liu, Y., and Xiao, L. (2024). Metamorphic evolution of the granulites and its geological implications in the Xinglong area of the eastern Hebei terrane, North Craton China. *Acta Petrol. Sin.* 40, 3398–3425. (in Chinese with English abstract). doi:10.18654/1000-0569/2024.11.05

Chu, H., Wang, H., Rong, G., Chang, Q., Kang, J., Jin, S., et al. (2016). The geological significance of the rediscovered fuchsite quartzite with abundant Eoarchean detrital zircons in Eastern Hebei Province. *Chin. Sci. Bull.* 6l, 2299–2308. doi:10.1360/N972015-00998

Collins, W. J., Van Kranendonk, M. J., and Teyssier, C. (1998). Partial convective overturn of archaean crust in the east pilbara craton, western Australia: driving mechanisms and tectonic implications. *J. Struct. Geol.* 20, 1405–1424. doi:10.1016/S0191-8141(98)00073-X

Condie, K. C. (1981). *Archean greenstone belts*. Amsterdam New York: Elsevier Scientific Pub. Co. Distributors for the U.S. and Canada, Elsevier North-Holland.

Cui, M., Zhang, L., Wu, H., Xu, Y., and Li, W. (2014). Timing and tectonic setting of the sijiaying banded iron deposit in the eastern hebei province, north China craton: constraints from geochemistry and SIMS zircon U–Pb dating. *J. Asian Earth Sci.* 94, 240–251. doi:10.1016/j.jseaes.2014.05.019

Cui, R., Wei, C., and Duan, Z. (2024). Metamorphic P–T paths and zircon U–Pb ages of neoarchean ultrahigh-temperature migmatitic granulites from the qingyuan terrane, north China craton. *Precambrian Res.* 404, 107345. doi:10.1016/j.precamres.2024.107345

Cutts, K. A., Stevens, G., Hoffmann, J. E., Buick, I. S., Frei, D., and Munker, C. (2014). Paleo-to mesoarchean polymetamorphism in the barberton granite-greenstone belt, South Africa: constraints from U–Pb monazite and Lu-Hf garnet geochronology on the tectonic processes that shaped the belt. *Geol. Soc. Am. Bull.* 126, 251–270. doi:10.1130/B30807.1

Diener, J. F. A., Stevens, G., Kisters, A. F. M., and Poujol, M. (2005). Metamorphism and exhumation of the basal parts of the barberton greenstone belt, South Africa: constraining the rates of mesoarchaean tectonism. *Precambrian Res.* 143, 87–112. doi:10.1016/j.precamres.2005.10.001

Dong, C., Liu, S., Nutman, A. P., Li, P., Xie, H., Li, Y., et al. (2024). New discovery of 3.84–3.64 Ga diverse granitoids in eastern hebei, north China craton: petrogenesis and significance. *Geol. Soc. Am. Bull.* 136, 5249–5261. doi:10.1130/B37553.1

Duan, Z., Wei, C., and Li, Z. (2019). Metamorphic P–T paths and zircon U–Pb ages of Paleoproterozoic metabasic dykes in eastern Hebei and northern Liaoning: implications for the tectonic evolution of the North China Craton. *Precambrian Res.* 326, 124–141. doi:10.1016/j.precamres.2017.11.001

Duan, Z., Wei, C., Li, Z., and Zhang, C. (2022). Zircon U–Pb dating and metamorphism of granitoid gneisses and supracrustal rocks in eastern hebei, north China craton. *Minerals* 12, 863. doi:10.3390/min12070863

Duan, Z., Wei, C., and Qian, J. (2015). Metamorphic P–T paths and Zircon U–Pb age data for the Paleoproterozoic metabasic dykes of high-pressure granulite

facies from Eastern Hebei, North China Craton. *Precambrian Res.* 271, 295–310. doi:10.1016/j.precamres.2015.10.015

Duan, Z., Wei, C., and Rehman, H. U. (2017). Metamorphic evolution and zircon ages of pelitic granulites in eastern hebei, north China craton: insights into the regional archean P–T–t history. *Precambrian Res.* 292, 240–257. doi:10.1016/j.precamres.2017.02.008

Dziggel, A., Knipfer, S., Kisters, A. F. M., and Meyer, F. M. (2006). *P–T* and structural evolution during exhumation of high- *T*, medium- *P* basement rocks in the barberton mountain land, South Africa. *J. Metamorph. Geol.* 24, 535–551. doi:10.1111/j.1525-1314.2006.00653.x

Foster, M. P. (1960). Interpretation of the composition of trioctahedral micas.

François, C., Philippot, P., Rey, P., and Rubatto, D. (2014). Burial and exhumation during archean sagduction in the east pilbara granite-greenstone terrane. *Earth Planet. Sci. Lett.* 396, 235–251. doi:10.1016/j.epsl.2014.04.025

Fu, J., Liu, S., Chen, X., Bai, X., Guo, R., and Wang, W. (2016). Petrogenesis of taxitic dioritic–tonalitic gneisses and neoarchean crustal growth in eastern hebei, north China craton. *Precambrian Res.* 284, 64–87. doi:10.1016/j.precamres.2016.08.002

Fu, J., Liu, S., Sun, G., and Gao, L. (2021). Two contrasting neoarchean metavolcanic rock suites in eastern hebei and their geodynamic implications for the northern north China craton. *Gondwana Res.* 95, 45–71. doi:10.1016/j.gr.2021.02.023

Fu, J., Liu, S., Wang, M., Chen, X., Guo, B., and Hu, F. (2017). Late neoarchean monzogranitic–syenogranitic gneisses in the eastern Hebei–Western liaoning province, north China craton: petrogenesis and implications for tectonic setting. *Precambrian Res.* 303, 392–413. doi:10.1016/j.precamres.2017.05.002

Gao, X., Wang, D., Huang, F., Wang, Y., and Wang, C. (2023). Chronolgy and geochemistry of the sijiaying iron deposit in eastern Hebei province, north China craton: implications for the genesis of high-grade iron ores. *Minerals* 13, 775. doi:10.3390/min13060775

Geng, Y., Liu, F., and Yang, C. (2006). Magmatic event at the end of the archean in eastern Hebei Province and its geological implication. *Acta Geol. Sin. - Engl. Ed.* 80, 819–833. doi:10.1111/j.1755-6724.2006.tb00305.x

Guo, R., Liu, S., Santosh, M., Li, Q., Bai, X., and Wang, W. (2013). Geochemistry, zircon U–Pb geochronology and Lu–Hf isotopes of metavolcanics from eastern Hebei reveal Neoarchean subduction tectonics in the North China Craton. *Gondwana Res.* 24, 664–686. doi:10.1016/j.gr.2012.12.025

Guo, R., Liu, S., Wyman, D., Bai, X., Wang, W., Yan, M., et al. (2015). Neoarchean subduction: a case study of arc volcanic rocks in qinglong-zhuzhangzi area of the eastern hebei province, north China craton. *Precambrian Res.* 264, 36–62. doi:10.1016/j.precamres.2015.04.007

Han, C., Xiao, W., Su, B., Chen, Z., Zhang, X., Ao, S., et al. (2014). Neoarchean algoma-type banded iron formations from eastern hebei, north China craton: SHRIMP U–Pb age, origin and tectonic setting. *Precambrian Res.* 251, 212–231. doi:10.1016/j.precamres.2014.06.019

Herron, M. M. (1988). Geochemical classification of terrigenous sands and shales from core or log data. *SEPM J. Sediment. Res.* 58. doi:10.1306/212F8E77-2B24-11D7-8648000102C1865D

Holland, T., and Powell, R. (2003). Activity-composition relations for phases in petrological calculations: an asymmetric multicomponent formulation. *Contrib. Mineral. Petrol.* 145, 492–501. doi:10.1007/s00410-003-0464-z

Holland, T. J. B., and Powell, R. (1998). An internally consistent thermodynamic data set for phases of petrological interest. *J. Metamorph. Geol.* 16, 309–343. doi:10.1111/j.1525-1314.1998.00140.x

Holland, T. J. B., and Powell, R. (2011). An improved and extended internally consistent thermodynamic dataset for phases of petrological interest, involving a new equation of state for solids: thermodynamic dataset for phases of petrological interest. *J. Metamorph. Geol.* 29, 333–383. doi:10.1111/j.1525-1314.2010.00923.x

Hu, Z., Li, X., Luo, T., Zhang, W., Crowley, J., Li, Q. L., et al. (2021). Tanz zircon megacrysts: a new zircon reference material for the microbeam determination of U–Pb ages and Zr–O isotopes. *J. Anal. At. Spectrom.* 36, 2715–2734. doi:10.1039/D1JA00311A

Jayananda, M., Banerjee, M., Pant, N. C., Dasgupta, S., Kano, T., Mahesha, N., et al. (2012). 2.62 Ga high-temperature metamorphism in the central part of the eastern dharwar craton: implications for late archaean tectonothermal history. *Geol. J.* 47, 213–236. doi:10.1002/gj.1308

Kusky, T., Huang, Y., Wang, L., Robinson, P. T., Wirth, R., Polat, A., et al. (2022). Vestiges of early earth's deep subduction and CHONSP cycle recorded in archean ophiolitic podiform chromitites. *Earth Sci. Rev.* 227, 103968. doi:10.1016/j.earscirev.2022.103968

Kusky, T. M., Polat, A., Windley, B. F., Burke, K. C., Dewey, J. F., Kidd, W. S. F., et al. (2016). Insights into the tectonic evolution of the north China craton through comparative tectonic analysis: a record of outward growth of precambrian continents. *Earth Sci. Rev.* 162, 387–432. doi:10.1016/j.earscirev.2016.09.002

Kwan, L. C. J., Zhao, G., Yin, C., and Geng, H. (2016). Metamorphic P–T path of mafic granulites from eastern hebei: implications for the neoarchean tectonics of the eastern block, north China craton. *Gondwana Res.* 37, 20–38. doi:10.1016/j.gr.2016.05.004

Li, Z., Wei, C., Yang, C., and Zhang, X. (2024). A deep mantle source for the late neoarchean metamorphosed basalts in eastern hebei, north China craton: insights from whole-rock geochemistry and Sm-Nd isotopes, and zircon U–Pb–Hf isotopes. *J. Earth Sci.* 35, 29–40. doi:10.1007/s12583-023-1807-5

Li, Z., Wei, C., Zhang, S., Yang, C., and Duan, Z. (2019). Neoarchean granitoid gneisses in eastern hebei, north China craton: revisited. *Precambrian Res.* 324, 62–85. doi:10.1016/j.precamres.2019.01.020

Lin, S., and Beakhouse, G. P. (2013). Synchronous vertical and horizontal tectonism at late stages of archean cratonization and genesis of hemlo gold deposit, superior craton, ontario, Canada. *Geology* 41, 359–362. doi:10.1130/G33887.1

Lin, S., Parks, J., Heaman, L. M., Simonetti, A., and Corkery, M. T. (2013). Diapirism and sagduction as a mechanism for deposition and burial of "timiskaming-type" sedimentary sequences, superior province: evidence from detrital zircon geochronology and implications for the borden lake conglomerate in the exposed middle to lower crust in the kapuskasing uplift. *Precambrian Res.* 238, 148–157. doi:10.1016/j.precamres.2013.09.012

Liou, P., Guo, J., Huang, G., and Fan, W. (2017). 2.9 Ga magmatism in eastern hebei, north China craton. *Precambrian Res.* 326, 6–23. doi:10.1016/j.precamres.2017.11.002

Liu, B., Neubauer, F., Liu, J., Jin, W., Li, W., and Liang, C. (2017). Neoarchean ductile deformation of the northeastern north China craton: the shuangshanzi ductile shear zone in qinglong, eastern hebei, north China. *J. Asian Earth Sci.* 139, 224–236. doi:10.1016/j.jseaes.2017.01.014

Liu, D. Y., Nutman, A. P., Compston, W., Wu, J. S., and Shen, Q. H. (1992). Remnants of ≥3800 ma crust in the chinese part of the Sino-korean craton. *Geology*, 20, 339. doi:10.1130/0091-7613(1992)020<0339:romcit>2.3.co;2

Liu, F., Liu, P., Wang, F., Liu, J., Meng, E., Cai, J., et al. (2014). U–Pb dating of zircons from granitic leucosomes in migmatites of the jiaobei terrane, southwestern jiao–liao–ji belt, north China craton: constraints on the timing and nature of partial melting. *Precambrian Res.* 245, 80–99. doi:10.1016/j.precamres.2014.01.001

Liu, J., Zhang, J., Liu, Z., Yin, C., Zhao, C., Li, Z., et al. (2018). Geochemical and geochronological study on the paleoproterozoic rock assemblage of the xiuyan region: new constraints on an integrated rift-and-collision tectonic process involving the evolution of the jiao-liao-ji belt, north China craton. *Precambrian Res.* 310, 179–197. doi:10.1016/j.precamres.2018.03.005

Liu, S., Wan, Y., Sun, H., Nutman, A. P., Xie, H., Dong, C., et al. (2013). Paleo- to eoarchean crustal evolution in eastern hebei, north China craton: new evidence from SHRIMP U–Pb dating and *in-situ* Hf isotopic study of detrital zircons from paragneisses. *J. Asian Earth Sci.* 78, 4–17. doi:10.1016/j.jseaes.2013.07.041

Liu, T., and Wei, C. (2018). Metamorphic evolution of Archean ultrahigh-temperature mafic granulites from the western margin of Qian'an gneiss dome, eastern Hebei Province, North China Craton: insights into the Archean tectonic regime. *Precambrian Res.* 318, 170–187. doi:10.1016/j.precamres.2018.10.007

Liu, T., and Wei, C. (2020). Metamorphic *P–T* paths and zircon U–Pb ages of archean ultra-high temperature paragneisses from the qian'an gneiss dome, east hebei terrane, north China craton. *J. Metamorph. Geol.* 38, 329–356. doi:10.1111/jmg.12524

Liu, T., Wei, C., and Johnson, T. E. (2024). Archean UHT metamorphism with counterclockwise P–T path: insights from pelitic granulites from east hebei, north China craton. *Gondwana Res.* 133, 108–128. doi:10.1016/j.gr.2024.06.007

Liu, T., Wei, C., Johnson, T. E., and Sizova, E. (2022). Newly-discovered ultra-high temperature granulites from the east hebei terrane, north China craton. *Sci. Bull.* 67, 670–673. doi:10.1016/j.scib.2021.12.023

Liu, T., Wei, C., Kröner, A., Han, B., and Duan, Z. (2020). Metamorphic P–T paths for the archean caozhuang supracrustal sequence, eastern hebei province, north China craton: implications for a sagduction regime. *Precambrian Res.* 340, 105346. doi:10.1016/j.precamres.2019.105346

Liu, Y., Hu, Z., Gao, S., Günther, D., Xu, J., Gao, C., et al. (2008). *In situ* analysis of major and trace elements of anhydrous minerals by LA-ICP-MS without applying an internal standard. *Chem. Geol.* 257, 34–43. doi:10.1016/j.chemgeo.2008.08.004

Lu, H., and Wei, C. (2020). Late neoarchean or late paleoproterozoic high-pressure granulite facies metamorphism from the east hebei terrane, north China craton? *J. Asian Earth Sci.* 190, 104195. doi:10.1016/j.jseaes.2019.104195

Lu, J., Zhai, M., Lu, L., and Zhao, L. (2017). P-T-t evolution of neoarchaean to paleoproterozoic pelitic granulites from the jidong terrane, eastern north China craton. *Precambrian Res.* 290, 1–15. doi:10.1016/j.precamres.2016.12.012

Ludwig, K. (2003). *ISOPLOT 3.0: a geochronological toolkit for Microsoft Excel.* Berkeley geochronology center special publication.

Lv, B., Zhai, M., Li, T., and Peng, P. (2012). Zircon U–Pb ages and geochemistry of the qinglong volcano-sedimentary rock series in eastern hebei: implication for ~2500Ma intra-continental rifting in the north China craton. *Precambrian Res.* 208–211, 145–160. doi:10.1016/j.precamres.2012.04.002

Ning, W., Kusky, T., Wang, L., and Huang, B. (2022). Archean eclogite-facies oceanic crust indicates modern-style plate tectonics. *Proc. Natl. Acad. Sci.* 119, e2117529119. doi:10.1073/pnas.2117529119

Ning, W., Kusky, T., Wang, L., Wang, J., Deng, H., Huang, B., et al. (2023). Neoarchean SSZ and MOR ultra-/high-pressure ophiolitic mélanges of the Eastern Hebei Complex,

North China Craton: dynamics of an Archean paleo-subduction zone. *Earth-Science Rev.* 240, 104403. doi:10.1016/j.earscirev.2023.104403

Nutman, A. P., Maciejowski, R., and Wan, Y. (2014). Protoliths of enigmatic archaean gneisses established from zircon inclusion studies: case study of the caozhuang quartzite, E. Hebei, China. *Geosci. Front.* 5, 445–455. doi:10.1016/j.gsf.2013.10.001

Nutman, A. P., Wan, Y., Du, L., Friend, C. R. L., Dong, C., Xie, H., et al. (2011). Multistage late neoarchaean crustal evolution of the north China craton, eastern hebei. *Precambrian Res.* 189, 43–65. doi:10.1016/j.precamres.2011.04.005

Sizova, E., Gerya, T., Brown, M., and Stüwe, K. (2018). What drives metamorphism in early archean greenstone belts? Insights from numerical modeling. *Tectonophysics* 746, 587–601. doi:10.1016/j.tecto.2017.07.020

Stevens, G. (2002). Amphibolite facies metamorphism in the schapenburg schist belt: a record of the mid-crustal response to 3.23 Ga terrane accretion in the barberton greenstone belt. *S. Afr. J. Geol.* 105, 271–284. doi:10.2113/1050271

Sun, H., Dong, C., Xie, H., Wang, W., Ma, M., Liu, D., et al. (2010). The Formation age of the Neoarchean zhuzhangzi and dantazi groups in the qinglong area Eastern Hebei Province: evidence from SHRIMP U–Pb zircon dating. *Geol. Rev.* 56, 888–898. doi:10.16509/j.georeview.2010.06.009

Sun, H., Xie, H., Liu, S., Dong, C., Liu, D., and Wan, Y. (2016). Archean magmatism and metamorphism in the Huangbaiyu Yangyashan area, eastern Hebei Province: evidence from SHRIMP zircon U–Pb dating. *Geol. Bull. China*. 35, 27–42. doi:10.12097/gbc.dztb-35-1-27

Sun, S., and McDonough, W. F. (1989). Chemical and isotopic systematics of oceanic basalts: implications for mantle composition and processes. *Geol. Soc. Lond. Spec. Publ.* 42, 313–345. doi:10.1144/GSL.SP.1989.042.01.19

Wan, Y., Liu, D., Dong, C., Xie, H., Kröner, A., Ma, M., et al. (2015). "Formation and evolution of archean continental crust of the north China craton," in *Precambrian Geology of China*. Editor M. Zhai (Berlin, Heidelberg: Springer Berlin Heidelberg), 59–136. doi:10.1007/978-3-662-47885-1_2

Wan, Y., Xie, H., Wang, H., Liu, S., Chu, H., Xiao, Z., et al. (2021). Discovery of early Eoarchen-Hadean zircons in eastern Hebei, North China Craton. *Acta Geol. Sin.* 95, 277–291. doi:10.19762/j.cnki.dizhixuebao.2021130

Wang, L., Wang, R., Ning, W., and Kusky, T. (2025). North China Archean dome-and-basin structures: arc plutons, superimposed folds, or sagduction? *Geology* 53 (6), 503–508. doi:10.1130/G53210.1

Wang, W., Liu, F.-L., Ji, L., and Santosh, M. (2019). Geochronology and geochemistry of the neoarchean lulong complex in the eastern hebei province, north China craton: implications on regional crustal evolution. *Precambrian Res.* 323, 102–125. doi:10.1016/j.precamres.2019.01.013

Wei, C., Zhai, M., and Wang, B. (2023). Four phases of orosirian metamorphism in the north north China craton (NNCC): insights into the regional tectonic framework and evolution. *Earth Sci. Rev.* 241, 104449. doi:10.1016/j.earscirev.2023.104449

White, P., and Holland, W. (2000). The effect of TiO_2 and Fe_2 O_3 on metapelitic assemblages at greenschist and amphibolite facies conditions: mineral equilibria calculations in the system K_2 O–FeO–MgO–Al_2 O_3 –SiO_2 –H_2 O–TiO_2 –Fe_2 O_3. *J. Metamorph. Geol.* 18, 497–511. doi:10.1046/j.1525-1314.2000.00269.x

White, R. W., Powell, R., and Johnson, T. E. (2014). The effect of Mn on mineral stability in metapelites revisited: new *a – x* relations for manganese-bearing minerals. *J. Metamorph. Geol.* 32, 809–828. doi:10.1111/jmg.12095

Wilde, S. A., Valley, J. W., Kita, N. T., Cavosie, A. J., and Liu, D. (2008). SHRIMP U–Pb and CAMECA 1280 oxygen isotope results from ancient detrital zircons in the caozhuang quartzite, eastern hebei, north China craton: evidence for crustal reworking 3.8 Ga ago. *Am. J. Sci.* 308, 185–199. doi:10.2475/03.2008.01

Wu, F., Yang, J., Liu, X., Li, T., Xie, L., and Yang, Y. (2005). Hf isotopes of the 3.8 Ga zircons in eastern hebei province, China: implications for early crustal evolution of the north China craton. *Chin. Sci. Bull.* 50, 2473. doi:10.1360/982005-629

Wu, H., Niu, X., Zhang, L., Pirajno, F., Luo, H., Qin, F., et al. (2015). Geology and geochemistry of the macheng algoma-type banded iron-formation, north China craton: constraints on mineralization events and genesis of high-grade iron ores. *J. Asian Earth Sci.* 113, 1179–1196. doi:10.1016/j.jseaes.2015.05.024

Wu, J., Geng, Y., Shen, Q., Wan, Y., Liu, D., and Song, B. (1998). *Archean geology characteristics and tectonic evolution of Sino-Korea paleo-continent*. Beijing: Geological Publication House. (in Chinese).

Wu, K., Zhao, G., Sun, M., Yin, C., He, Y., and Tam, Y. (2013). Metamorphism of the northern liaoning complex: implications for the tectonic evolution of neoarchean basement of the eastern block, north China craton. *Geosci. Front.* 4, 305–320. doi:10.1016/j.gsf.2012.11.005

Wu, Y., and Zheng, Y. (2004). 锆石成因矿物学研究及其对U-Pb年龄解释的制约. *Chin. Sci. Bull.* 49, 1589–1604. (in Chinese). doi:10.1360/csb2004-49-16-1589

Wu, Z., Wang, C., Allen, M. B., Tang, M., Chen, Y., Jia, L., et al. (2024). Rise of mantle oxidation by neoarchean subduction in the north China craton. *Earth Planet. Sci. Lett.* 646, 119006. doi:10.1016/j.epsl.2024.119006

Wu, Z., Wang, C., Song, S., Allen, M. B., Kusky, T., and Su, L. (2022). Ultrahigh-pressure peridotites record neoarchean collisional tectonics. *Earth Planet. Sci. Lett.* 596, 117787. doi:10.1016/j.epsl.2022.117787

Xiang, H., and Connolly, J. A. D. (2021). GeoPS: an interactive visual computing tool for thermodynamic modelling of phase equilibria. *J. Metamorph. Geol.* 40, 243–255. doi:10.1111/jmg.12626

Xu, N., Zhao, G., Zhang, H. C. G., and Yao, J. (2022). Metamorphic P-T paths and zircon U–Pb ages of the intermediate to felsic granulites from the jianping complex, the north China craton:implications for the neoarchean tectonic regime. *Lithos* 424–425, 106754. doi:10.1016/j.lithos.2022.106754

Yang, C., and Wei, C. (2017a). Two phases of granulite facies metamorphism during the neoarchean and paleoproterozoic in the east hebei, north China craton: records from mafic granulites. *Precambrian Res.* 301, 49–64. doi:10.1016/j.precamres.2017.09.005

Yang, C., and Wei, C. (2017b). Ultrahigh temperature (UHT) mafic granulites in the east hebei, north China craton: constraints from a comparison between temperatures derived from REE-based thermometers and major element-based thermometers. *Gondwana Res.* 46, 156–169. doi:10.1016/j.gr.2017.02.017

Yang, J., Wu, F., Wilde, S., and Zhao, G. (2008). Petrogenesis and geodynamics of late archean magmatism in eastern hebei, eastern north China craton: geochronological, geochemical and Nd–Hf isotopic evidence. *Precambrian Res.* 167, 125–149. doi:10.1016/j.precamres.2008.07.004

Yu, C., Yang, T., Zhang, J., Zhao, G., Cawood, P. A., Yin, C., et al. (2022). Coexisting diverse P–T–t paths during neoarchean sagduction: insights from numerical modeling and applications to the eastern north China craton. *Earth Planet. Sci. Lett.* 586, 117529. doi:10.1016/j.epsl.2022.117529

Zhai, M. (2011). Cratonization and the Ancient North China Continent: a summary and review. *Sci. China Earth Sci.* 54, 1110–1120. (in Chinese). doi:10.1007/s11430-011-4250-x

Zhai, M., and Santosh, M. (2011). The early precambrian odyssey of the north China craton: a synoptic overview. *Gondwana Res.* 20, 6–25. doi:10.1016/j.gr.2011.02.005

Zhang, J., Zhao, G. C., Shen, W. L., Li, S. Z., and Sun, M. (2015). Aeromagnetic study of the Hengshan–Wutai–Fuping region: unraveling a crustal profile of the Paleoproterozoic Trans-North China Orogen. *Tectonophysics* 662, 208–218. doi:10.1016/j.tecto.2015.08.025

Zhang, J., Zhao, G. C., Shen, W. L., Li, S. Z., Sun, M., Chan, L. S., et al. (2012). Structural and aeromagnetic studies of the Wutai Complex: implications for the tectonic evolution of the Trans-North China Orogen. *Precambrian Res.* 222–223, 212–229. doi:10.1016/j.precamres.2011.08.009

Zhang, L., Zhai, M., Zhang, X., Xiang, P., Dai, Y., Wang, C., et al. (2012). Formation age and tectonic setting of the shirengou neoarchean banded iron deposit in eastern hebei province: constraints from geochemistry and SIMS zircon U–Pb dating. *Precambrian Res.* 222–223, 325–338. doi:10.1016/j.precamres.2011.09.007

Zhang, X., Zhai, M., Zhao, L., Zhou, Y., and Liou, P. (2024). Ultrahigh-temperature crustal anatexis and final cratonization in eastern hebei, north China craton: insights from ca. 2.46 Ga taipingzhai enderbites. *Geol. Soc. Am. Bull.* 136, 4913–4935. doi:10.1130/B37319.1

Zhao, C., Liu, J., Zhang, H., Zhang, C., Chen, J., Cui, D., et al. (2025). Low-pressure ~3.53 Ga trondhjemite in the Eastern Hebei: Implications on the coitinental nucleus formation of the North China Craton. *Precambrian Res.* 417, 107668. doi:10.1016/j.precamres.2024.107668

Zhao, C., Zhang, J., Wang, X., Zhang, C., Chen, G., Zhang, S., et al. (2023). Tracing the early crustal evolution of the north China craton: new constraints from the geochronology and Hf isotopes of fuchsite quartzite in the lulong area, eastern hebei province. *Minerals* 13, 1174. doi:10.3390/min13091174

Zhao, C., Zhang, J., Zhao, G., Yin, C., Chen, G., Liu, J., et al. (2021). Kinematics and structural evolution of the anziling dome-and-keel architecture in east China: evidence of neoarchean vertical tectonism in the north China craton. *GSA Bull.* 134, 2115–2129. doi:10.1130/B36225.1

Zhao, G. (2014). *Precambrian evolution of the north China craton*. Amsterdam: Elsevier.

Zhao, G., Cawood, P. A., Li, S., Wilde, S. A., Sun, M., Zhang, J., et al. (2012). Amalgamation of the north China craton: key issues and discussion. *Precambrian Res.* 222–223, 55–76. doi:10.1016/j.precamres.2012.09.016

Zhao, G., Sun, M., Wilde, S. A., and Sanzhong, L. (2005). Late archean to paleoproterozoic evolution of the north China craton: key issues revisited. *Precambrian Res.* 136, 177–202. doi:10.1016/j.precamres.2004.10.002

Zhao, G., Wilde, S. A., Cawood, P. A., and Lu, L. (1998). Thermal evolution of archean basement rocks from the eastern part of the north China craton and its bearing on tectonic setting. *Int. Geol. Rev.* 40, 706–721. doi:10.1080/00206819809465233

Zhao, G., Wilde, S. A., Cawood, P. A., and Lu, L. (1999). Thermal evolution of two textural types of mafic granulites in the north China craton: evidence for both mantle plume and collisional tectonics. *Geol. Mag.* 136, 223–240. doi:10.1017/S001675689900254X

Zhao, G., and Zhai, M. (2013). Lithotectonic elements of precambrian basement in the north China craton: review and tectonic implications. *Gondwana Res.* 23, 1207–1240. doi:10.1016/j.gr.2012.08.016

Zou, Y., Chu, X., Wu, J., and Zhao, L. (2022). No evidence for archean eclogite-facies metamorphism. *Proc. Natl. Acad. Sci.* 119, e2208090119. doi:10.1073/pnas.2208090119